Biomedical Optics EXPRESS

Enhanced robustness digital holographic microscopy for demanding environment of space biology

M. Fatih Toy,[1*] Stéphane Richard,[2] Jonas Kühn,[1,3] Alfredo Franco-Obregón,[2] Marcel Egli,[2] and Christian Depeursinge[1]

[1]*École Polytechnique Fédérale de Lausanne (EPFL), Advanced Photonics Laboratory, CH-1015, Lausanne, Switzerland*
[2]*Eidgenössische Technische Hochschule Zurich, Space Biology Group, CH-8005, Zurich, Switzerland*
[3]*École Polytechnique Fédérale de Lausanne (EPFL), Biomolecular Screening Facility, CH-1015, Lausanne, Switzerland*
**fatih.toy@epfl.ch*

Abstract: We describe an optimized digital holographic microscopy system (DHM) suitable for high-resolution visualization of living cells under conditions of altered macroscopic mechanical forces such as those that arise from changes in gravitational force. Experiments were performed on both a ground-based microgravity simulation platform known as the random positioning machine (RPM) as well as during a parabolic flight campaign (PFC). Under these conditions the DHM system proved to be robust and reliable. In addition, the stability of the system during disturbances in gravitational force was further enhanced by implementing post-processing algorithms that best exploit the intrinsic advantages of DHM for hologram autofocusing and subsequent image registration. Preliminary results obtained in the form of series of phase images point towards sensible changes of cytoarchitecture under states of altered gravity.

OCIS codes: (090.1995) Digital holography; (180.0180) Microscopy; (180.2520) Fluorescence microscopy.

References and links

1. G. Clément and K. Slenzka, *Fundamentals of Space Biology. Research on Cells, Animals, and Plants in Space* (Microcosm Press, El Segundo, CA, and Springer, New York, 2006).
2. N. J. Penley, C. P. Schafer, and J.-D. F. Bartoe, "The International Space Station as a microgravity research platform," Acta Astronaut. **50**(11), 691–696 (2002).
3. V. A. Thomas, N. S. Prasad, and C. A. M. Reddy, "Microgravity research platforms—a study," Curr. Sci. **79**, 336–340 (2000).
4. M. Cogoli, "The fast rotating clinostat: a history of its use in gravitational biology and a comparison of ground-based and flight experiment results," ASGSB Bull. **5**(2), 59–67 (1992).
5. Y. Ohira, T. Yoshinaga, T. Nomura, F. Kawano, A. Ishihara, I. Nonaka, R. R. Roy, and V. R. Edgerton, "Gravitational unloading effects on muscle fiber size, phenotype and myonuclear number," Adv. Space Res. **30**(4), 777–781 (2002).
6. H. Rösner, T. Wassermann, W. Möller, and W. Hanke, "Effects of altered gravity on the actin and microtubule cytoskeleton of human SH-SY5Y neuroblastoma cells," Protoplasma **229**(2-4), 225–234 (2006).
7. J. Blum, G. Wurm, S. Kempf, T. Poppe, H. Klahr, T. Kozasa, M. Rott, T. Henning, J. Dorschner, R. Schräpler, H. U. Keller, W. J. Markiewicz, I. Mann, B. A. Gustafson, F. Giovane, D. Neuhaus, H. Fechtig, E. Grün, B. Feuerbacher, H. Kochan, L. Ratke, A. El Goresy, G. Morfill, S. J. Weidenschilling, G. Schwehm, K. Metzler, and W. H. Ip, "Growth and form of planetary seedlings: results from a microgravity aggregation experiment," Phys. Rev. Lett. **85**(12), 2426–2429 (2000).
8. U. L. D. Friedrich, O. Joop, C. Pütz, and G. Willich, "The slow rotating centrifuge microscope NIZEMI--a versatile instrument for terrestrial hypergravity and space microgravity research in biology and materials science," J. Biotechnol. **47**(2-3), 225–238 (1996).
9. M. S. Whorton, J. T. Eldridge, R. C. Ferebee, J. O. Lassiter, and J. W. Redmon, Jr., "Damping mechanisms for microgravity vibration isolation," MSFC Center Director's Discretionary Fund Final Report, Project No. 94–07, NASA/TM-1998–206953 (NASA, 1998).

#156744 - $15.00 USD Received 25 Oct 2011; revised 6 Jan 2012; accepted 12 Jan 2012; published 13 Jan 2012

10. P. B. Jacquemin, D. Laurin, S. Atalick, R. McLeod, S. Lai, and R. A. Herring, "Non-intrusive, three-dimensional temperature and composition measurements inside fluid cells in microgravity using a confocal holography microscope," Acta Astronaut. **60**(8-9), 723–727 (2007).
11. G. Reibaldi, P. Manieri, H. Mundorf, R. Nasca, and H. K. Sonig, "The European Multi-User Facilities for the Columbus Laboratory," ESA Bull. **102**, 107–120 (2002).
12. K. Lang, C. Strell, B. Niggemann, K. S. Zänker, A. Hilliger, F. Engelmann, and O. Ullrich, "Real-time video-microscopy of migrating immune cells in altered gravity during parabolic flights," Microgravity Sci. Technol. **22**(1), 63–69 (2010).
13. F. Dubois, L. Joannes, O. Dupont, J. L. Dewandel, and J. C. Legros, "An integrated optical set-up for fluid-physics experiments under microgravity conditions," Meas. Sci. Technol. **10**(10), 934–945 (1999).
14. U. Schnars, K. Sommer, B. Grubert, H. J. Hartmann, and W. Juptner, "Holographic diagnostics of fluid experiments onboard the International Space Station," Meas. Sci. Technol. **10**(10), 900–903 (1999).
15. F. Dubois, N. Callens, C. Yourassowsky, M. Hoyos, P. Kurowski, and O. Monnom, "Digital holographic microscopy with reduced spatial coherence for three-dimensional particle flow analysis," Appl. Opt. **45**(5), 864–871 (2006).
16. F. Prodi, G. Santachiara, S. Travaini, F. Belosi, A. Vedernikov, F. Dubois, P. Queeckers, and J. C. Legros, "Digital holography for observing aerosol particles undergoing Brownian motion in microgravity conditions," Atmos. Res. **82**(1-2), 379–384 (2006).
17. E. Cuche, P. Marquet, and C. Depeursinge, "Simultaneous amplitude-contrast and quantitative phase-contrast microscopy by numerical reconstruction of Fresnel off-axis holograms," Appl. Opt. **38**(34), 6994–7001 (1999).
18. T. Colomb, E. Cuche, F. Charrière, J. Kühn, N. Aspert, F. Montfort, P. Marquet, and C. Depeursinge, "Automatic procedure for aberration compensation in digital holographic microscopy and applications to specimen shape compensation," Appl. Opt. **45**(5), 851–863 (2006).
19. P. Ferraro, S. De Nicola, A. Finizio, G. Coppola, S. Grilli, C. Magro, and G. Pierattini, "Compensation of the inherent wave front curvature in digital holographic coherent microscopy for quantitative phase-contrast imaging," Appl. Opt. **42**(11), 1938–1946 (2003).
20. P. Marquet, B. Rappaz, P. J. Magistretti, E. Cuche, Y. Emery, T. Colomb, and C. Depeursinge, "Digital holographic microscopy: a noninvasive contrast imaging technique allowing quantitative visualization of living cells with subwavelength axial accuracy," Opt. Lett. **30**(5), 468–470 (2005).
21. B. Kemper, D. Carl, J. Schnekenburger, I. Bredebusch, M. Schäfer, W. Domschke, and G. von Bally, "Investigation of living pancreas tumor cells by digital holographic microscopy," J. Biomed. Opt. **11**(3), 034005 (2006).
22. D. Gabor, "A new microscopic principle," Nature **161**(4098), 777–778 (1948).
23. E. N. Leith and J. Upatniek, "Reconstructed Wavefronts and Communication Theory," J. Opt. Soc. Am. **52**(10), 1123–1128 (1962).
24. J. W. Goodman and R. W. Lawrence, "Digital image formation from electronically detected holograms," Appl. Phys. Lett. **11**(3), 77–79 (1967).
25. M. A. Kronrod, N. S. Merzlyakov, and L. P. Yaroslavskii, "Reconstruction of a hologram with a computer," Sov. Phys. Tech. Phys. **17**, 333–334 (1972).
26. W. S. Haddad, D. Cullen, J. C. Solem, J. W. Longworth, A. McPherson, K. Boyer, and C. K. Rhodes, "Fourier-transform holographic microscope," Appl. Opt. **31**(24), 4973–4978 (1992).
27. K. Boyer, J. C. Solem, J. W. Longworth, A. B. Borisov, and C. K. Rhodes, "Biomedical three-dimensional holographic microimaging at visible, ultraviolet and X-ray wavelengths," Nat. Med. **2**(8), 939–941 (1996).
28. E. Cuche, F. Bevilacqua, and C. Depeursinge, "Digital holography for quantitative phase-contrast imaging," Opt. Lett. **24**(5), 291–293 (1999).
29. C. P. McElhinney, B. M. Hennelly, and T. J. Naughton, "Extended focused imaging for digital holograms of macroscopic three-dimensional objects," Appl. Opt. **47**(19), D71–D79 (2008).
30. T. Colomb, N. Pavillon, J. Kühn, E. Cuche, C. Depeursinge, and Y. Emery, "Extended depth-of-focus by digital holographic microscopy," Opt. Lett. **35**(11), 1840–1842 (2010).
31. P. Ferraro, S. Grilli, D. Alfieri, S. De Nicola, A. Finizio, G. Pierattini, B. Javidi, G. Coppola, and V. Striano, "Extended focused image in microscopy by digital Holography," Opt. Express **13**(18), 6738–6749 (2005).
32. M. Antkowiak, N. Callens, C. Yourassowsky, and F. Dubois, "Extended focused imaging of a microparticle field with digital holographic microscopy," Opt. Lett. **33**(14), 1626–1628 (2008).
33. T. Hoson, S. Kamisaka, Y. Masuda, and M. Yamashita, "Changes in plant prowth processes under microgravity conditions simulated by a three-dimensional clinostat," J. Plant Res. **105**(1), 53–70 (1992).
34. A. G. Borst and J. W. A. van Loon, "Techonlogy and developments for the random positioning machine, RPM," Microgravity Sci. Technol. **21**(4), 287–292 (2009).
35. C. S. Simmons, J. Y. Sim, P. Baechtold, A. Gonzalez, C. Chung, N. Borghi, and B. L. Pruitt, "Integrated strain array for cellular mechanobiology studies," J. Micromech. Microeng. **21**(5), 054016 (2011).
36. V. Pletser, "Short duration microgravity experiments in physical and life sciences during parabolic flights: the first 30 ESA campaigns," Acta Astronaut. **55**(10), 829–854 (2004).
37. C. Pache, J. Kühn, K. Westphal, M. F. Toy, J. M. Parent, O. Büchi, A. Franco-Obregón, C. Depeursinge, and M. Egli, "Digital holographic microscopy real-time monitoring of cytoarchitectural alterations during simulated microgravity," J. Biomed. Opt. **15**(2), 026021 (2010).
38. P. Langehanenberg, B. Kemper, D. Dirksen, and G. von Bally, "Autofocusing in digital holographic phase contrast microscopy on pure phase objects for live cell imaging," Appl. Opt. **47**(19), D176–D182 (2008).
39. M. Liebling and M. Unser, "Autofocus for digital Fresnel holograms by use of a Fresnelet-sparsity criterion," J. Opt. Soc. Am. A **21**(12), 2424–2430 (2004).

#156744 - $15.00 USD Received 25 Oct 2011; revised 6 Jan 2012; accepted 12 Jan 2012; published 13 Jan 2012

40. R. P. Brent, *Algorithms for Minimization without Derivatives* (Dover, New York, 2002).
41. B. Zitova and J. Flusser, "Image registration methods: a survey," Image Vis. Comput. **21**(11), 977–1000 (2003).
42. F. Charrière, B. Rappaz, J. Kühn, T. Colomb, P. Marquet, and C. Depeursinge, "Influence of shot noise on phase measurement accuracy in digital holographic microscopy," Opt. Express **15**(14), 8818–8831 (2007).
43. E. De Castro and C. Morandi, "Registration of translated and rotated images using finite fourier transforms," IEEE Trans. Pattern Anal. Mach. Intell. **PAMI-9**(5), 700–703 (1987).
44. M. Guizar-Sicairos, S. T. Thurman, and J. R. Fienup, "Efficient subpixel image registration algorithms," Opt. Lett. **33**(2), 156–158 (2008).
45. B. Städler, T. M. Blättler, and A. Franco-Obregón, "Time-lapse imaging of in vitro myogenesis using atomic force microscopy," J. Microsc. **237**(1), 63–69 (2010).

1. Introduction

The extraterrestrial space environment exhibiting reduced gravity and cosmic radiations has attracted the attention of scientists as it holds the answer as to how life evolved on earth. The research fields of space biology and space medicine were largely inspired because of the growing number of human space flights. The aim of early experiments in Space research was to elucidate the effect of microgravity not only on individual cells, but also on the intact organism. Experiments have shown that some of the effects of reduced gravity are permanent, whereas others persist only temporarily. Later, with the development of space research platforms, the interest of researchers shifted to the biological mechanisms underlying the observed effects induced by microgravity.

We are using the low gravity environment during spaceflights as a model environment to study cellular processes involved in mechanotransduction [1]. The challenges of conducting such studies are not only getting access to the limited opportunities on microgravity platforms such as parabolic flights, sounding rockets or space flights, but also to design and build experiment hardware suitable for the low-gravity environment and the travel there, defining appropriate procedure for sample handling, as well as conducting sufficient experimental repeats for the subsequent statistical analysis [2]. Nevertheless, spaceflight can be substituted to a large extent by ground-based microgravity simulation platforms such as fast rotating clinostats or 3D clinorotation (for instance, by using a random positioning machine, RPM) or sub-orbital flights (such as parabolic flight campaigns, high altitude balloon drops, and sounding rockets) [3,4].

Early attempts at understanding the effects of microgravity over cell behavior consisted of exposing cells to reduced gravity and next microscopically observing their cytoarchitectural responses post-chemical fixation [5,6]. In fact, optical microscopes were applied in microgravity research most often in the field of physical sciences. These early in situ studies commonly used low numerical aperture (NA) microscope objectives with moderate magnification levels. Poor imaging performance of these microscopes was also the basis of their intrinsic robustness against environmental vibrations [7,8] but later on vibration isolation systems became a requirement with the demand of high NA microscopes. Due to the nature of the vibration spectrum, passive systems are not sufficient to isolate low frequency disturbances. Hence, active isolation systems are employed for such cases [9,10]. With an increased demand for sophisticated experimental instruments, such isolation systems were implemented on-board the International Space Station (ISS) for microscopic experiments [11]. However, the complexity and cost of these isolation systems hamper their use for microgravity experiments.

Various light microscopy modalities have been facilitated in microgravity studies. These imaging modalities include classical bright field [7], dark field [8], epifluorescence [12], confocal [10], and interference microscopy techniques [8,10,13–16]. Digital holographic microscopy (DHM), a branch of interference microscopy, has been utilized on various microgravity platforms for flow physics and protein crystal growth experiments [13–16]. However, they offer low NA with matching magnification (Max: 0.3NA, 20X) making them insufficient for other applications. In this paper, a digital holographic microscope with epifluorescence microscopy mode is presented for space biology studies at the single cell level. This DH microscope offers superior NA and magnification without vibration isolation. Epifluorescence microscopy facilitates the observation of labeled intracellular structures

#156744 - $15.00 USD Received 25 Oct 2011; revised 6 Jan 2012; accepted 12 Jan 2012; published 13 Jan 2012

before and after the experiments by eliminating the need of a second microscope. Microscope operation without vibration isolation is enabled by the inherent advantages of DHM implicit to numerical focusing [17], numerical aberration correction [18,19], label free operation [20,21], and short exposure time. Methods incorporating these advantages in the post-processing for the enhanced robustness of the microscope are discussed as a substitute for vibration isolation. Additionally, initial live cell imaging results from the tests on microgravity platforms are provided.

2. Methods and experimental setup

2.1. Digital holographic microscopy (DHM)

Originally, holography is a wave field encoding technique composed of recording and reconstruction steps. Recording of a hologram is accomplished by the coherent addition of the wave field to be encoded (Object field) to a known wave field (Reference field) and exposing a photochemical plate to the resulting intensity pattern [22]. In this pattern, intensity terms from object and reference wave coexist with the cross terms of a wave field and complex conjugate of the remaining one. Illumination of the exposed plate by the same reference wave emerges the object wave with other terms in hologram reconstruction. Mixing up the object wave with other terms in the reconstruction step can be prevented by the off-axis recording scheme [23]. For this type of hologram recording, an angle is simply introduced between the reference and object waves incident to the recording plate. The selection of the optimum angle depends on two parameters, optical resolution of the photochemical plate and the desired resolution of the object reconstruction.

DHM replaces the photochemical plate by a digital camera, the hologram reconstruction is done numerically [24,25] and finally, a microscope objective is introduced on the path of the object wave to maximize the collected spatial frequencies [26,27]. The off-axis recording angle is optimized to allow the recording of entire object wave frequencies based on the camera pixel size and the NA of the microscope objective in use [28]. Moving into numerical reconstruction, off-axis recording scheme allows the Fourier filtering of object wave. After this step, the Fresnel propagation approximation is applied to numerically reconstruct the wave field at a desired distance which is also called as digital focusing. The amplitude and quantitative phase information of the object is acquired from this propagated wave field [17]. The resulting quantitative phase image is a function of either topography or integrated optical path length (OPL) of the object based on the Michelson or Mach-Zehnder interferometer type hologram recording geometry. In transmission geometry, OPL is the integrated refractive index mismatch in axial direction and apparent in the measured quantitative phase map, φ(x,y), as

$$\varphi(x,y) = 2\pi \frac{OPL(x,y)}{\lambda} = 2\pi \frac{\left[n_c(x,y) - n_{em}\right] d(x,y)}{\lambda} \tag{1}$$

where n_c is the intracellular refractive index, n_{em} refractive index of the extracellular medium, and d the cell thickness, for live cell imaging [20]. Measured quantitative phase map is proportional to cell topography under the strict assumption of a homogeneous intracellular refractive index (n_c = constant) which has a different value than the surrounding medium. However, many cell types break this assumption with protein rich intracellular sites where local refractive index is higher than the rest of the cell. Eventually, both cell morphology and refractive index distribution are expressed together in the measured phase signal.

Digital focusing capability of DHM is a crucial advantage that is not only limited to the case of objects with axial dimensions larger than the depth of field (DOF) of the imaging system, which is defined as

$$DOF = \frac{\lambda n_m}{NA^2} \tag{2}$$

#156744 - $15.00 USD Received 25 Oct 2011; revised 6 Jan 2012; accepted 12 Jan 2012; published 13 Jan 2012

where n_m stands for the refractive index of the immersion medium [29–31]. This extension of DOF also enables the imaging of particles that are mobile in axial direction [16,32]. Extended DOF capability of the technique combined with numerical autofocusing holds a great potential for imaging applications requiring high NA under harsh mechanical disturbances. Exploration of this potential for our application is further explained in section 3.1. Another important core advantage of the technique is the numerical aberration compensation [18,19]. With the help of fitted polynomials on the phase at hologram plane, it is possible to compensate for wave front curvature mismatches and slight misalignment of optical elements. In general, such artifacts have a static nature, but the methods are also applicable to cases where aberrations change dynamically. Considering the shock and vibration environment of microgravity experiments, one can expect some level of deflection, bending, and backlash of opto-mechanical elements. All these mechanical reactions are reflected on holograms as aberrations, and compensation for aberration on every hologram independently is sufficient to overcome this problem.

2.2. Microgravity platforms

The RPM and parabolic flight campaign (PFC) were employed to test the performance of the microscope. The RPM was developed by Dutch Space, formerly Fokker Space, Leiden, the Netherlands. The RPM is essentially a 3D clinostat, in which the gravity vector is continually reoriented allowing simulating microgravity conditions. Microgravity is produced by the RPM via the principle of time averaged nullification of gravity vector [33,34]. Probes are fixed as close as possible to the center of two frames rotating one inside the other. Driven by separate motors, the rotation of each frame is random and autonomous and regulated by computer software.

Such a rotating machine provides a challenging environment for any optical-mechanical setup since loading condition on mechanics continuously changes in case of constant velocity. Accelerations and rotation direction changes dramatize the condition by introducing mechanical shocks. All these disturbances happen at low frequencies where most isolation systems fail. Excluding mechanical issues, RPM is an ideal experimental platform with a sufficiently large experimental volume ($50x50x50cm^3$) for a microscopy system and offers built-in signal and power transmission to the experiment. In the experiments described here, the angular velocity of rotation was 60°/s. The temperature was maintained at 37°C. The simulation lasted from 10 minutes to 1 hour. C2C12 cells were seeded at low density in perfusion chambers (CoverWell, #622503) tightened by glass coverslips (Menzel-Gläser, BB024050A1). The C2C12 mouse muscle cell line (ATCC number: CRL-1772) is an accepted cell system for the study of cellular mechanotransduction [35]. A mechano-chemical chain of events recruiting calcium homeostasis, extracellular matrix modifications, and cytoskeletal dynamics governs cellular mechanotransduction. The study of this cell line during brief exposures to low gravity will contribute to the understanding of the factors producing muscle atrophy (mitigated regeneration) during space travel.

The second microgravity platform for the microscope testing is the parabolic flight that creates real microgravity conditions for a short duration of approximately 20 seconds [36]. Parabolic flights for research purposes are carried out by NASA, Novespace (for CNES, DLR, ESA, JAXA, and NASA), Zero-G Corp, Russian Atlas Aerospace, and Ecuadorian Air Force. The performance of our microscope setup was tested during ESA's 53rd PFC operated by Novespace in October 2010. This campaign included three flight days of each 31 parabolic flight maneuvers. A maneuver starts with a steady flight at the cruising altitude of approximately 6'000m above mean sea level (AMSL). Then the plane (Airbus A-300) starts to climb up until the nose angle reaches 47°. During this 20 seconds pull-up phase, 1.8-2g of hypergravity is experienced. At the end of this phase, the engine thrust is minimized just to overcome the air drag without introducing acceleration. The plane then follows a parabolic free fall trajectory for 20-25 seconds during which gravity is neutralized (microgravity phase). When the diving nose angle reaches 42°, the engines are turned on again to stabilize the flight. This pull-out phase takes about 20 seconds during which the gravity raises up to 1.8g. A

#156744 - $15.00 USD Received 25 Oct 2011; revised 6 Jan 2012; accepted 12 Jan 2012; published 13 Jan 2012

parabola maneuver is illustrated in Fig. 1 with corresponding gravity levels and durations. Experimental setups on board the Airbus A 300 have to be enclosed in structural profile frames and tightly fixed to plane floor. This fixation causes a transfer of all shocks and vibrations not only during flight but also during taxi, takeoff, and landing.

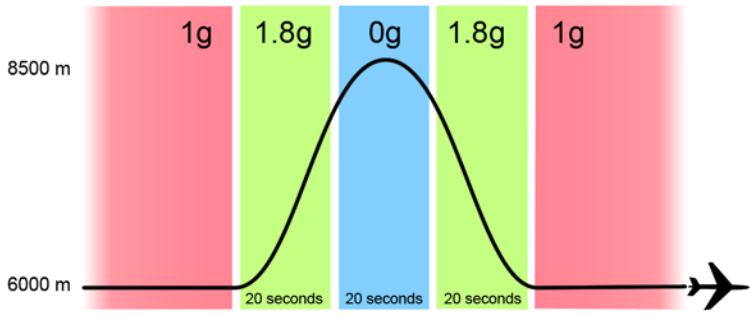

Fig. 1. Illustration of a single parabola flight maneuver during PFCs indicating the different gravity levels

2.3. Experimental setup

An early version of the DH microscope that was operable on RPM [37] was upgraded to enclose a DHM and a widefield epifluorescence microscopy module that operates in time sequential manner. The inclusion of a fluorescence microscopy module enables experimenters to observe fluorophore labeled structures in a steady state environment in comparison to phase images. When DHM mode operation is activated, the collimated beam from the laser diode is divided into two arms by a beam splitter. The reference wave with a wave front curvature matching the object wave is expanded by optics and directed to a dichroic beam splitter as illustrated in Fig. 2a. Meanwhile the object wave passes through a condenser lens, cell sample, microscope objective (60X, 0.85NA, LOMO #OB-QPA60), and the dichroic beam splitter consecutively, before reaching the Andor Luca electron multiplying CCD (EMCCD) camera. Dichroic beam splitter is selected to have a suitable spectral response (cut-off wavelength at 500nm, 85/15 at laser diode wavelength of 653nm) to be used for both fluorescence and DHM.

A light emitting diode (LED) serves as the excitation source for the epifluorescence microscopy mode. This LED has the central wavelength of 470nm with 30nm of spectral bandwidth that places it as a compatible source for fluorophores having blue excitation, such as enhanced Green Fluorescent Protein (eGFP) and Fluo-4. The illumination shape of the LED is controlled by a bi-convex lens and a diaphragm placed after it. The uniformed illumination beam passes through the short pass excitation filter ($\lambda^{exc}_{cut\text{-}off}$ = 500nm), gets reflected by the dichroic filter and excites the sample fluorophores through the microscope objective. Fluorescence emission is collected and imaged on the camera through the dichroic filter and long pass emission filter ($\lambda^{em}_{cut\text{-}off}$ = 500nm) by the microscope objective. Figure 2a shows the optical schematic of the microscope.

Mainly off the shelf opto-mechanical mounting elements are chosen for the mechanical construction of this microscope. All of the optical components of the microscope excluding the microscope objective and EMCCD camera are mounted in to 30mm standard cage plates from Thorlabs Inc. and joined using the cage rods from the same supplier. Such a mechanical construction provides mechanical rigidity with the movement of elements constrained to be in single axis. After the positioning cage plates, each cage plate is fixed to the cage rods using the locking screws and to the microscope body on an orthogonal plane. Sample positioning stages, microscope objective, and EMCCD camera are mounted to the microscope body through custom brackets and flanges.

#156744 - $15.00 USD Received 25 Oct 2011; revised 6 Jan 2012; accepted 12 Jan 2012; published 13 Jan 2012

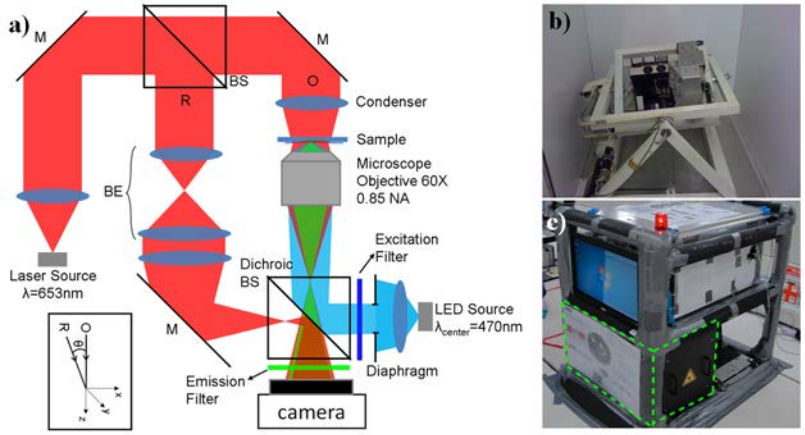

Fig. 2. (a) Schematic of the microscope with the inset showing off-axis recording where M: Mirror, BS: Beam Splitter, BE: Beam Expander, R: Reference Beam, and O: Object Beam, (b) picture of the microscope on RPM (Media 1), and (c) picture of the experimental rack on plane (microscope is enclosed in the bottom shelf of the rack where highlighted by green dashed lines)

The microscope is accommodated on RPM with other peripheral instruments as shown in Fig. 2b and Media 1. Microscope and peripheral instruments are mounted on custom carrier plates that are fixed to the inner frame of the RPM. Overall weight of the system reaches to 13.21kg with the center of weight 69mm away from the center of rotation. Any rotational instability arising from this distance is prevented by the introduction of a 2.9kg steel block as a counterweight. Among the peripheral instruments, the experimental computer stores acquired images and controls the switching between light sources for DHM and fluorescence microscopy mode operation. For previewing needs, experimental computer is linked to an external computer via Wi-Fi link. Acquired holograms and fluorescence images are streamed to the external computer. Phase images are reconstructed on this external computer. In order to avoid slow acquisition speed, streaming of the holograms to the external computer is stopped before the experiments and images are recorded locally with an acquisition speed of 1 frame/second. Later on, stored images are post-processed in offline mode.

Regarding the PFC, the microscope and other experimental instruments are fixed on the bottom shelf of an experimental rack (Fig. 2c). The microscope is enclosed inside a containment box as mandated by the flight safety regulations. After the takeoff of the plane, the microscope is switched on, and hologram and fluorescence image acquisition carried out for the entire flight including all sequences of the parabola maneuvers as well as the parabola breaks in-between. Similar to the RPM experiments, images stored on a flash drive are reconstructed and post-processed later.

3. Post-processing

Harsh environmental conditions such as those confronted on the RPM or during parabolic flights impact severely on the mechanical stability and functioning of a microscope and manifest themselves as the axial and lateral drift of the sample and acquired images. The constantly changing angle of the gravitational force exerted on the microscope during the rotation on RPM and the fluctuation of the gravitational force acting on the system during parabolic flight in conjunction with the shocks and vibrations occurring during RPM rotation direction changes and PFC plane maneuvers are the main reasons for the drift. The digital focusing capability afforded by the numerical propagation of DHM allows for autofocusing image correction with registration algorithms to overcome the axial drift and lateral displacements.

In case of large number of holograms to be autofocused and reconstructed in offline scheme, computational load as well as the focus accuracy becomes critical parameters for the

#156744 - $15.00 USD Received 25 Oct 2011; revised 6 Jan 2012; accepted 12 Jan 2012; published 13 Jan 2012

proposed autofocusing approach. Digital hologram autofocusing as an optimization problem is intended to find the extremum of a unimodal or multimodal sharpness metric [38,39]. Based on the selection of the sharpness metric one needs to use a proper method to find the minima. In general, multimodal metrics require larger number of iterations to isolate the global minima. In comparison, unimodal sharpness metric brings the advantages of faster convergence, easier implementation, and the absence of local minima traps. Various sharpness metrics are chosen from the literature and applied on experimental holograms of C2C12 mouse myoblast cells, which are mainly phase objects [38]. For a large propagation interval of 30cm in the image space, these sharpness metrics are evaluated with 0.3mm sampling steps and visualized in Fig. 3a. This range is chosen to be larger than any possible autofocus distance, enabling the treatment of two extreme points of the range as the optimization boundaries. In the figure 'Spec' corresponds to summation of logarithmically weighted power spectra inside the pass region of propagated field's Fourier transform. This sharpness metric is mathematically expressed in Eq. (3) where pass region is defined by a DC blocking mask $M(u,v)$ with spectral coordinates u and v, and $O(x,y)$ denotes the complex field at a propagation distance. Variance of the grayscale amplitude distribution of the propagated field is stated as 'Var' in Eq. (4). In this equation N_x and N_y stand for the spatial pixel counts. Cumulative edges in the amplitude of the propagated field as criteria for image sharpness are calculated in both first derivatives approximation or gradient 'Gra', Eq. (5), and second derivatives approximation or Laplacian 'Lap', Eq. (6). Referring back to Fig. 3a, all of these metrics but the variance behave as multimodal functions, whereas variance appears as a suitable candidate sharpness metric with its unimodal behavior:

$$Spec = \sum_{u,v} \log\{1 + [M(u,v) \circ FFT(|O(x,y)|)]\} \tag{3}$$

$$Var = \frac{1}{N_x N_y} \sum_{x,y} [|O(x,y)| - \overline{|O(x,y)|}]^2 \tag{4}$$

$$Grad = \sum_{x=1}^{N_x-1} \sum_{y=1}^{N_y-1} \sqrt{[|O(x,y)| - |O(x-1,y)|]^2 + [|O(x,y)| - |O(x,y-1)|]^2} \tag{5}$$

$$\begin{aligned} Lap = \sum_{x=1}^{N_x-1} \sum_{y=1}^{N_y-1} [&|O(x+1,y)| + |O(x-1,y)| \\ &+ |O(x,y+1)| + |O(x,y-1)| - 4|O(x,y)|]^2 \end{aligned} \tag{6}$$

All of the metrics that are in use for sharpness evaluation are expected to reach their minimum at the same axial position. However, considering the higher sensitivity to noise for some methods (e.g. 'Gra') experimental results from different methods may not converge to the same position. Zoomed inset in Fig. 3a shows the degree of discrepancy of evaluated metrics. Assuming that this discrepancy reflects the accuracy of autofocusing, the range of ambiguity can be calculated as 1.5mm, which is the autofocus distance difference between the 'Var' and 'Lap' metrics. Taking into account the axial magnification, which equates to the square of lateral magnification of 60X, introduced by the microscope objective, one can estimate the accuracy of the autofocusing in the object space as 0.42μm, and DOF is calculated to be 0.91μm using Eq. (2). Hence, such a range of ambiguity falling inside the DOF distance is not likely to pose any problem for the autofocusing procedure.

Considering the advantages of search methods for unimodal metrics, the only suitable metric, 'Var', is chosen as the sharpness metric. Accuracy of this sharpness metric is experimentally tested with the help of a motorized stage controlling the axial position of the object. For the axial positions ranging from –20μm to 20μm with the center being the physical imaging condition, holograms are acquired and best focus plane is found using the 'Var'

#156744 - $15.00 USD Received 25 Oct 2011; revised 6 Jan 2012; accepted 12 Jan 2012; published 13 Jan 2012

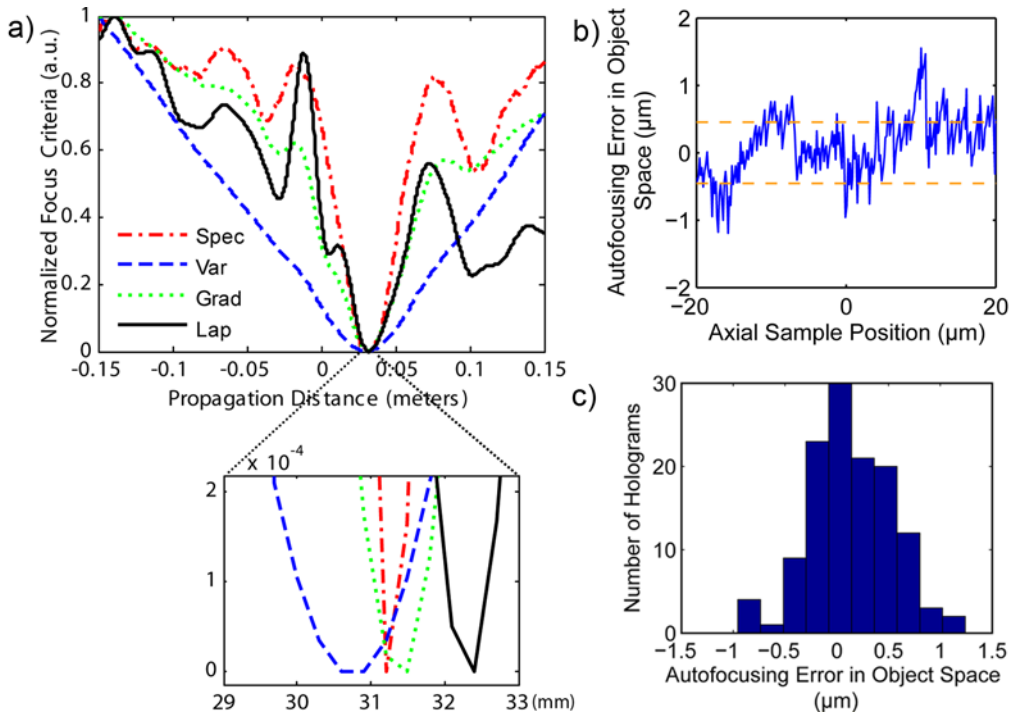

Fig. 3. (a) Comparison of several focus criteria in a propagation distance range of 30cm for an experimental hologram of cell. All criteria excluding variance of amplitude (Var) exhibit a multimodal behavior. Zoomed in inset shows the sharpness ambiguity of plotted criteria. (b) Plot and (c) histogram of the experimentally evaluated autofocusing error of 'Var' in object space for various axial sample positions with the center being the physical imaging condition (dashed orange lines indicate ± DOF/2).

criteria. Autofocusing distances in the image space are converted to object space by applying the thin lens approximation for the microscope objective. Calculated object space autofocusing distances are subtracted from the physical distance monitored from the motorized stage to end up with the accuracy of the autofocusing and shown in Fig. 3b. The plotted accuracy is comparable to the DOF indicated by the dashed orange lines. Positioning errors of the motorized stage and thin lens approximation of the microscope objective can also be additionally responsible for the increase of error with the large distances. For an easier evaluation, histogram of this autofocusing error is shown in Fig. 3c and clearly proves that the errors mostly stay below the DOF. In order to minimize iteration steps with sufficient confidence regions, the Brent's method was chosen as the search method [40]. By applying this method, the golden section search or parabola fitting is chosen to select the following iteration variable based on a test in predefined bounds. With the choice of variance and Brent's method as the metric and search method, autofocusing approach is implemented in the Matlab environment. For experimental holograms with 30cm of propagation range, convergence of the approach is obtained after 10-15 iteration steps. In order to speed up the autofocusing approach, iterative propagation is not applied on the holograms of 1024X1024 pixels but on a central region of 512X512 pixels instead. Green blocks of the flowchart given in Fig. 4 summarize the main steps involved in the autofocusing. With all steps included in autofocusing before the reconstruction of full size hologram, performance of the approach averages to 0.45 seconds per hologram on a mid-level workstation PC (Intel Core 2 Duo E8400 CPU at 3.00 GHz, 3.25 GB RAM, Windows XP 32 Bits, Matlab R2009b).

Following the autofocusing step, phase images are constructed from propagated numerical fields and fed into the next step of post-processing: the image registration. Image registration methodologies superimpose multiple images of the same object taken under different

#156744 - $15.00 USD Received 25 Oct 2011; revised 6 Jan 2012; accepted 12 Jan 2012; published 13 Jan 2012

conditions (illumination, zoom, viewpoint, etc.). In general, these methodologies are composed from three main steps as feature detection, feature matching, and transformation. However, its implementation can be quite different depending on the imaging modality, acquisition conditions, and desired transformation model [41]. In our case, mechanical disturbances caused translational movement of the field-of-view (FOV). Consequently, the transformation model is required to avoid transformation estimation errors. Moreover, the type of images to be registered plays an important role in defining the feature selection and matching algorithms. Phase map images constructed from numerical fields suffer from a certain degree of temporally varying parasitic noise arising from acquisition conditions [42]. Such a temporally varying pattern potentially degrades the performance of spatial feature matching algorithms. Furthermore, phase image DC level estimation (i.e. phase offset) errors and mobile particles inside the sample chamber, e.g. protein aggregates, negatively influence their performance. Hence, Fourier domain phase correlation based image registration algorithms are more suitable with their robustness to aforementioned issues [43]. In spite of its robustness, Fourier domain phase correlation methods bring a computational burden for subpixel registration cases with the requirement of inversely proportional fast Fourier transform (FFT) sample number per dimension. An extension to this class of image registration algorithms removes the computational burden by the use of discrete Fourier transforms (DFT) for the refining of initial cross-correlation peak estimation [44]. The implementation of this algorithm is employed for the registration of phase images. Within the algorithm, cross correlation peak of reference image and image to be registered is estimated from classical Fourier domain method with the upsampling factor of 2 for inverse FFT step. Then this initial estimate is refined by upsampled DFTs defined in a small window centered to the initial estimate. Furthermore, normalized value of the final cross correlation peak provides an estimation of registration quality. Since the modulus of this value increases with the similarity between two images, it is possible to use the difference between unity and the modulus of normalized cross correlation peak as an error metric of image registration. In the

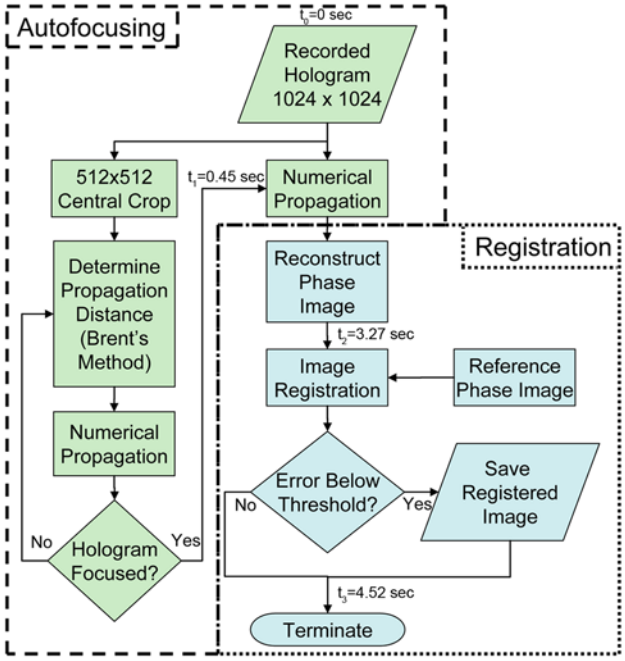

Fig. 4. Flowchart illustrating the post-processing steps. Functional blocks of digital hologram autofocusing are shown with green fill color, and phase image registration steps have blue fill color. Average computation times (referenced to t_0) at various checkpoints are also indicated.

#156744 - $15.00 USD Received 25 Oct 2011; revised 6 Jan 2012; accepted 12 Jan 2012; published 13 Jan 2012

implementation, a registered phase image quality is evaluated based on this error metric. An error threshold is experimentally chosen based on the registration of a set of images, in which threshold is located between the mean error metric of successfully and unsuccessfully registered images. In the use scenario, images with error below this threshold are saved, while others are ignored. General outline of the registration part of the post-processing is visualized in Fig. 4 with blue functional blocks.

Performance of the post-processing methodology is evaluated on experimental holograms of living C2C12 mouse myoblast cells acquired on the RPM platform. Three sample holograms are selected, one from the resting RPM condition and others during RPM rotation. For visualization purposes, phase images corresponding to these holograms are reconstructed at the acquisition plane with separate numerical aberration correction. Figures 5a, e, and i show these phase images with a colorbar at the bottom. The first phase image (Fig. 5a) corresponds to a hologram acquired when RPM was at rest position. Sharpness of the thin cell extend indicated by white arrow proves that the hologram is already in focus with no propagation (propagation distance of zero meters). Defocusing and lateral movement of the sample due to RPM rotation is observable on two other phase images with white arrows (Figs. 5e and i). As it can be concluded from these two images, degree of defocusing and amount of lateral movement vary dynamically during rotation. Phase images reconstructed after autofocusing are shown in the second column of the figure. One can assess the functionality of autofocusing from the comparison of Figs. 5f and j to Figs. 5e and i. Output of the last step of post-processing, image registration is shown in the third column of images. In addition, FOV cropping and histogram stretching are applied after image registration for the elimination of registration boundaries and to best use the dynamic range. On top of these

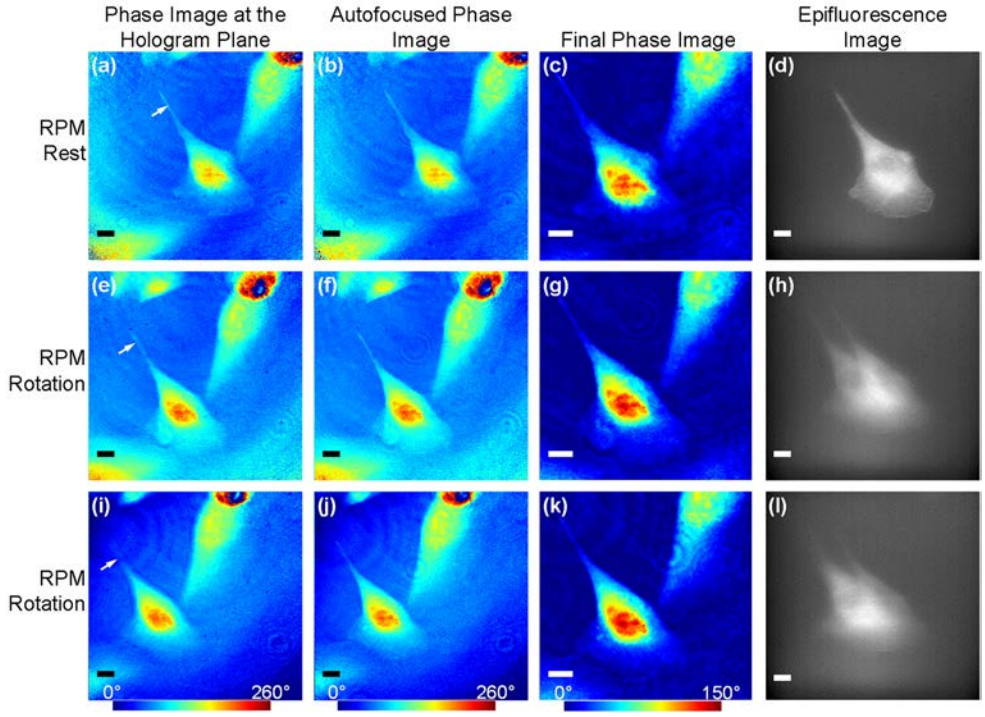

Fig. 5. Imaging of living C2C12 cells expressing eGFP tagged actin on the RPM platform (phase and fluorescence). Phase images with (a) no propagation, (b) after autofocusing, and (c) final registration output are shown for the RPM at rest (d) Fluorescence microscopy mode image after hologram acquisition is shown for comparison. (e-l) Phase images constructed from two holograms and corresponding fluorescence images during RPM rotation show the performance of our proposed post-processing. (Scalebars: 10μm). White arrows on the first column of images points to the cell extent where defocus is best observed.

#156744 - $15.00 USD Received 25 Oct 2011; revised 6 Jan 2012; accepted 12 Jan 2012; published 13 Jan 2012

phase images, raw fluorescence microscopy images of the eGFP transfected actin filaments captured after the hologram acquisitions are shown in the last column. Disturbances, which are corrected for the DHM mode, are easily shown on these images with the poor sharpness and motion blur worsen by the consequence of longer exposure time of a second.

4. Results

The system was applied to observe the morphological effects of gravitational unloading on C2C12 mouse myoblasts. For this purpose, eGFP-actin expressing C2C12 myoblasts were plated on glass coverslips and enclosed in the imaging chamber with Dulbecco's modified eagle medium (DMEM) containing 20% fetal calf serum (FCS). The RPM environmental temperature was kept constant at 37°C. For control purposes, DHM holograms of myoblasts and fluorescence images of the actin cytoskeletal network were recorded for about 30 minutes before switching on the RPM. For the recording of the alterations of the actin cytoskeleton during simulated microgravity, the RPM was paused just before taking fluorescence microscopic images at 5 minutes intervals. DHM mode and fluorescence microscopy mode acquisitions were conducted for 20-30 minutes under simulated microgravity conditions. All acquired holograms along with the fluorescence microscopy mode images were transferred to a workstation for the post-processing. Finally, movies were constructed from time series phase and fluorescence images. Four frames from a cell response movie (Media 2) are shown in Fig. 6. Here DHM mode phase images and fluorescence microscopy actin eGFP images are represented together for direct comparison.

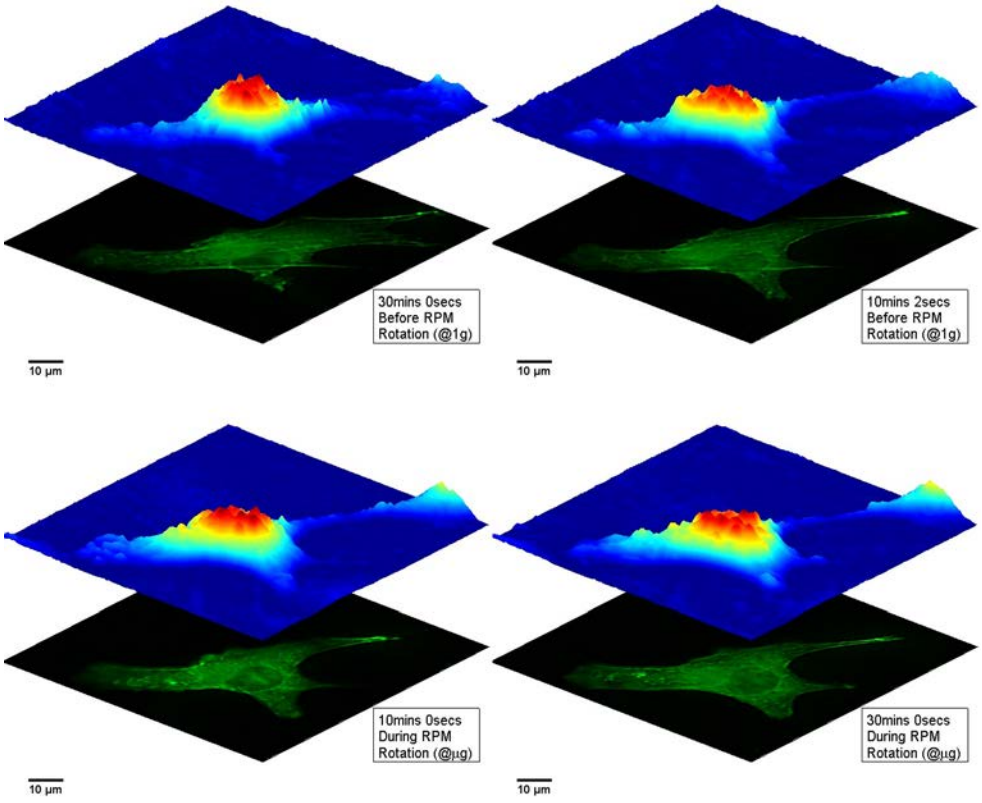

Fig. 6. Four frames extracted from DHM Phase and Fluorescence movie (Media 2), top row from 1g control and bottom row from RPM simulated microgravity. Phase images are located at the top respective image in a false color pseudo 3D format, while fluorescence microscopy images are beneath. At every frame, relative time to the control to microgravity transition is indicated with the gravity level

#156744 - $15.00 USD Received 25 Oct 2011; revised 6 Jan 2012; accepted 12 Jan 2012; published 13 Jan 2012

In the movie a cell expressing eGFP-actin filaments is observed at the center of the FOV, whereas another myoblast not expressing eGFP-actin sit outside the FOV (upper right) and hence, is not visible in the fluorescence image series. During the microgravity simulation particles existing in the cell medium gain mobility. These mobile particles pass through the FOV numerous times, but the effect on the image registration quality is negligible. Upon analyzing the fluorescence microscopy images it was noticeable that bright mobile spots moved centrally towards nucleus under the influence of simulated microgravity. Moreover, the system of actin stress fibers dispersed in response to the reduced environmental mechanical force imparted by simulated microgravity on the RPM. The doubling time of C2C12 myoblasts is between 13 and 15 hours; of this time approximately 2 hours is spent undergoing cytokinesis and 6 hours in undertaking DNA synthesis [45]. The amount of time that C2C12 myoblasts are within the G1 phase of the cell cycle and hence, most migratory is between 5 and 8 hours. In this respect, the degree and rate of changes we observed in the actin cytoskeleton in response to simulated microgravity is greater than that observed during normal cell migration. Monitoring the phase images in parallel also reveals that the phase signal is altered locally, in agreement with earlier findings [37]. Variation of the phase in the perinuclear region is also detected. suggesting that the cytosol and associated organellar structure also change distribution in response to reduced gravitational force. In addition, spontaneous protrusions of the membranes are observed at different locations along the cell periphery under 1g loading and microgravity. Considering that these are only preliminary observations without statistical confirmation, future studies on a larger number of cells will be needed to fully place these observations into context of undertaken cellular adaptations to altered environmental mechanical conditions, and subsequent biological results will be subject of a following publication.

The same cells are used (C2C12) for the on-board experiments during the ESA's 53rd PFC. After take-off, the system is activated, and the hologram recording is started as soon as the first cell of interest is centered inside the FOV. Due to the experimental limitation mentioned earlier, we exclusively used the DHM mode of the microscope. Given the short duration of different gravity levels during the flight (around 20 seconds), only fast response can be studied at this stage. Similar to the approach followed for the experiments on RPM, acquired holograms are post-processed after the flight and movies are generated like in Media 3. Focusing solely on the perinuclear phase variations, plots are generated and synchronized to the accelerometer data that was acquired by the flight operator. The graph provided in Media 3 and Fig. 7 may hint to a tiny effect that grows with successive parabolas flown. During the 5 minutes pause between sets of parabolas, the phase value appears to recover to its initial state as indicated by the black dashed line on the graph. With the following parabola set, an increase of similar form is observed again in the perinuclear phase.

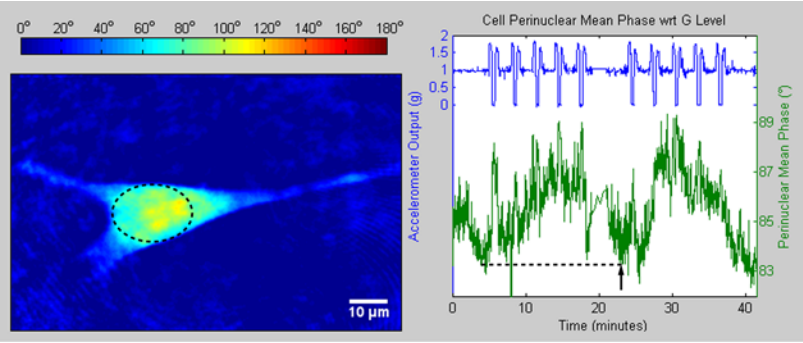

Fig. 7. DHM Phase movie (Media 3) of a cell acquired during ESA 53rd PFC. Left) False color phase image with reference color bar (top) in degrees. Right) Dynamic phase variation plot in a central region of the cell (indicated with dashed circle) with respect to the instantaneous gravity level. Black dashed line indicates to baseline phase value before the parabola set, and recovery to this value occurs at the end of the parabola set break marked by the arrow.

#156744 - $15.00 USD Received 25 Oct 2011; revised 6 Jan 2012; accepted 12 Jan 2012; published 13 Jan 2012

This increase in the perinuclear phase is close to the noise level and lacks confirmation by a large number of cells at this stage, preventing to draw conclusions. Riding over the accumulated effect of parabolas, individual parabola maneuvers also increase the measured perinuclear phase value during periods of microgravity in the seconds range. However, disturbances can also create a similar type of effect of the same measured order. Additional experiments are necessary to further explore the underlying mechanisms of this effect.

5. Conclusions

Here we present a transmission type digital holographic microscope with time sequential epifluorescence microscopy capability for space biology applications. The system enables the observation of transient morphological alteration of cells in harsh environmental conditions by taking advantage of the intrinsic capabilities of DHM. Disturbances of imaging performance are largely corrected by applying a simple and robust autofocusing algorithm followed by an image registration routine on DHM phase images. Also, integrated fluorescence microscopy provides a direct comparison of labeled intracellular architectures to correspondent DHM phase images. The DHM system was utilized on two different microgravity platforms; RPM (ground-based) and PFC. Experiments dedicated to morphological observation of mouse myoblast cells on these platforms proved the microscope to be robust, but also provided preliminary observations on the effect of gravitational unloading on myoblast cells. Future work involving detailed analysis and interpretation of the phase response collected from a large number of cells with statistical significance is to be undertaken in the next phases of the project.

Acknowledgments

The authors thank the EPFL Space Research Programme (ESRP) for the financial support. Furthermore, we thank the European Space Agency (ESA) for the opportunity to participate in the parabolic flight campaigns as well as Novespace for the organization of the parabolic flights and for their assistance. We acknowledge the technical help of Lyncée tec (www.lynceetec.com) as well as the fruitful discussions with them.

#156744 - $15.00 USD Received 25 Oct 2011; revised 6 Jan 2012; accepted 12 Jan 2012; published 13 Jan 2012